Near Field Measurement of a Fractal Antenna Using Fluorescence Thermography

Raphael Flor, Stéphane Fauré, Jean-François Bobo, Daniel Prost

Near Field Measurement of a Fractal Antenna Using Fluorescence Thermography

Raphaël Flor, Stéphane Fauré, Jean-François Bobo and Daniel Prost

***Abstract*—Measuring the near-field emitted by an antenna is essential for diagnosing its proper functioning and identifying any manufacturing defects. Unlike scanning systems that incrementally move a point sensor, electromagnetic (EM) field thermography enables rapid mapping of a surface in just a few seconds. Developed at ONERA under the name EMIR, infrared (IR) thermography involves heating a thin film with EM radiation. An IR camera measures this heating, which is proportional to the EM power density, thereby revealing the field amplitude.**

More recently, a new thermography technique derived from EMIR has been introduced. This method involves coating the thin film with a fluorophore. The fluorescence intensity, which depends on temperature and thus on the field, allows for mapping of the EM field using a simple optical camera.

Following a brief introduction to this method, we present its application to the measurement of a fractal antenna, which has also been numerically simulated.

***Index Terms*—Antenna Diagnosis, Non-Destructive Testing, Fluorescence Thermography, Fractal Antenna.**

I. Introduction

THE advent of microwave technologies, such as GPS, mobile communications, remote sensing, and their applications in various fields from aeronautics to medicine, highlights the growing importance of electromagnetic (EM) interactions in our environment. These complex interactions require a deep understanding of the involved EM fields, posing significant challenges in terms of their measurement and imaging. This is crucial not only for optimizing the performance of existing technologies, but also for anticipating and minimizing their potential adverse effects (electromagnetic compatibility). Conventional methods for field measurement and visualization on a 2D plane, such as the use of EM probes with scanning systems [1], have several limitations: acquisition time (depending on the number of measurement points), intrusiveness (particularly in reactive and very near field regions), and probe dimensions (typically close to wavelength). While probe arrays offer faster acquisition speeds, they are constrained by limited spatial resolution [2, 3]. Nevertheless, some of these methods are effective and commercially available [4, 5]. Optical measurements could also provide EM field visualization, but only on very small (~1 cm²) surfaces and require a complex microscopic test bench [6, 7]. The EM-Infrared method [8, 9], initially developed by ONERA [10] and now commercialized by ANYFIELDS [11], is an interesting alternative to these methods: a thin film is slightly heated by the EM field, and reveals the field map thanks to the infrared camera recording.

In this work, we exploit the modification of the fluorescent emission of the same thin film when coated with a heat-sensitive deposit, which can be recorded by a visible light camera [12-14]. This latter technique, known as fluorescence thermography, has been recently improved and can now provide near-field antenna patterns. It relies on the use of films slightly absorbing EM fields, coupled with a temperature-sensitive fluorophore. The EM energy absorbed by the film is converted to heat by Joule losses, leading to a variation in fluorescence intensity. This variation, correlated to the amplitude of the field, is recorded and analyzed. A modulation of the signal associated with a synchronous demodulation of the images eliminates continuous thermal drifts and spurious phenomena, which could otherwise compromise the fidelity of field visualization: this is called lock-in thermography and is also used in the infrared thermography method [15]. This technique allows visualizing EM maps, on a large 2D scale, and can be used for field leakage detection (in the context of electromagnetic compatibility), or for antenna characterization. In this article, we present the special case of a broadband fractal antenna, but any antenna could be measured in the same way, since thermography is not frequency-dependent. The simulation of this antenna is presented in paragraph §II; some details on the measurement method are given in paragraph §III and results, including comparison with simulation, are presented in paragraph §IV.

II. Simulation of the Antenna

The fractal antenna is a commercially available planar-type antenna. It is a mono-pole structure in which the metallic element is replaced by a succession of triangles organized in a fractal pattern (Fig. 1), enabling emission over a wide frequency band (1 to 10 GHz), but with preferential frequencies. A full description of such a multiband Sierpinski fractal antenna is given in [16]. Moreover, the behavior and particularly the scaling properties of the antenna's active region have been measured using infrared thermography at

This article was submitted on May 23, 2024.

R. Flor and S. Fauré are with ANYFIELDS, F-31200, Toulouse, France (e-mail : raphael.flor@anyfields.eu, stephane.faure@anyfields.eu).

J. F. Bobo is with CNRS/CEMES, F-31400, Toulouse, France (e-mail: jean-francois.bobo@cemes.fr).

D. Prost is with ONERA/DEMR, Université de Toulouse, F-31055 Toulouse, France (e-mail: daniel.prost@onera.fr).

Corresponding author: Daniel Prost

various frequencies [17]. In the referenced work, thermograms were obtained directly on the substrate, thus revealing current distribution patterns due to Joule heating (while the present work focuses on electric field distribution).

The structure is here symmetrically printed on both sides of an epoxy substrate (FR4 material, with a relative permittivity $\varepsilon_r = 4.4$). We simulated the antenna with the finite element method, using the commercial software HFSS.

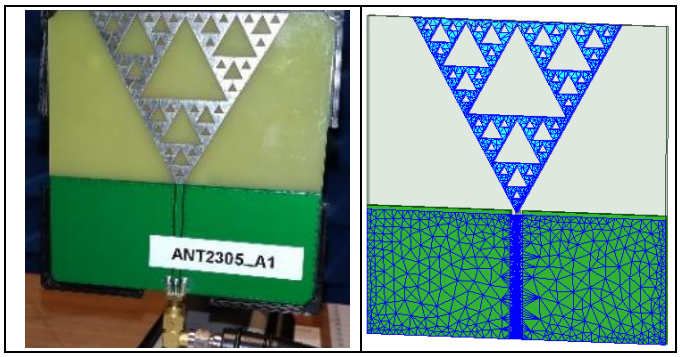

Fig. 1. Fractal antenna and HFSS meshing (metallic parts). The active fractal area is 60 mm high and wide, while the substrate dimension is 100 x 100 mm².

A. *S11 simulation and VNA validation*

Before performing thermography measurements, we verified the antenna performance through S-parameter measurements using a network analyzer. The measurement at S11 broadly confirms the simulation, validating the numerical model, although the second peak is not found at the same level (likely due to geometric inaccuracies due to manufacturing rough tolerances). We also verified that the presence of the thin film (located 10 mm from the antenna surface) did not alter the antenna behavior (Fig. 2), insofar as, even though the S11 value is slightly different, the peak frequencies remain the same with or without the film:

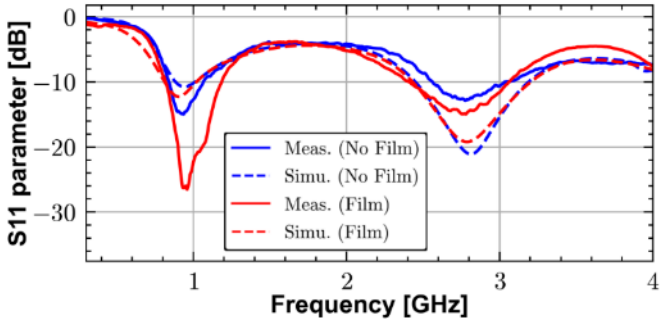

Fig. 2. S11 parameter as a function of frequency. 0.96 and 2.68 GHz correspond to highest efficiency of the antenna.

B. *Simulation of the near and far-field*

Even though the S11 behavior is indicative of the very low influence of the thin film, we have represented it as a surface impedance in the numerical model (Fig. 3), in order to check its influence on the near and far field patterns. The radiation pattern exhibits expected symmetrical behavior in azimuth ($\varphi = 90°$) and a 3 dB maximum gain in elevation at 20° (Fig. 4). With the film, a slight decrease in gain is observed, which corresponds to the portion of power absorbed by the film (converted into heat). However, neither the shape of the radiation diagram nor the near-field pattern is affected (Fig. 5). This guarantees that we measure a representative pattern of the antenna near and far radiated field.

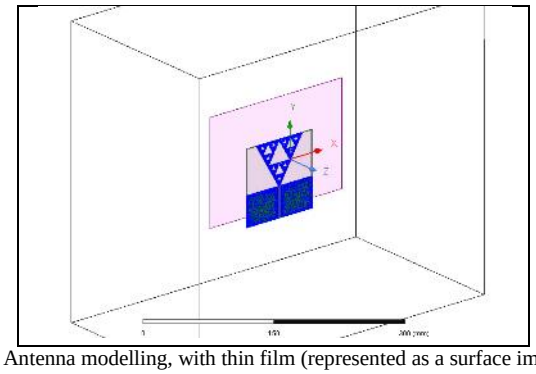

Fig. 3. Antenna modelling, with thin film (represented as a surface impedance with dimensions 200 x 140mm²) behind; radiation boundary conditions are applied on air-box walls (large square box).

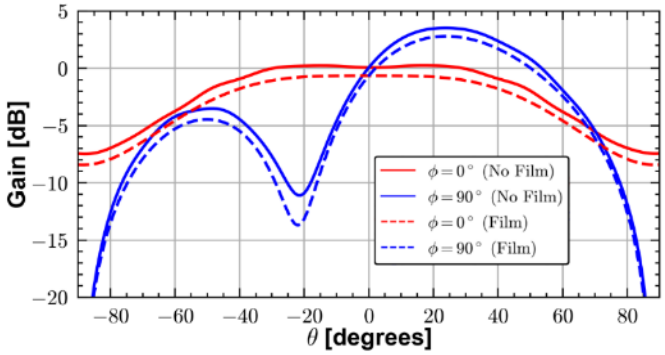

Fig. 4. Simulated radiation pattern with and without thin film (*f = 2.68 GHz).*

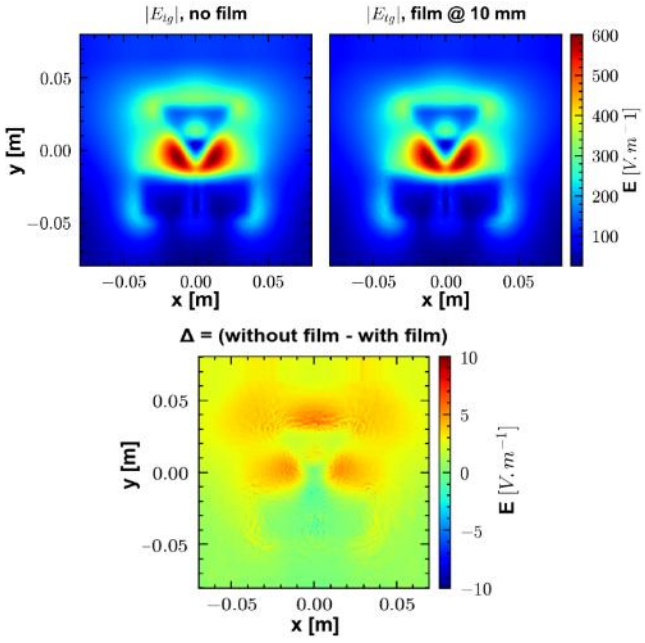

Fig. 5. Simulated electric near-field pattern $|E_{tg}|$ (tangent to the film component) with and without thin film (*f = 2.68 GHz*).

Even if the antenna gain is slightly reduced (by 0.5 to 1 dB), the shape of the radiation pattern remains unaffected, and the near-field pattern is only slightly affected. Figure 5 shows the difference, which reaches a few V/m in areas of interest where the measured field corresponds to hundreds of V/m. This

guarantees that we measure a representative pattern of the antenna near and far radiated field.

III. Method of Measurement

The thin film on which the fluorophore (rhodamine B) is deposited has a very low conductivity, represented by its surface resistance (or resistance per square) $Z_s = 1/\sigma e$, where e is the film thickness and σ its conductivity. With a surface resistance of a few thousand ohms, the film absorbs almost 10 % of the incident power, and this absorbed power is proportional to the square of the electric field amplitude E:

$$P_{abs} = \frac{E^2}{2Z_s} \quad (1)$$

This energy is converted into heat. As the source is switched on or off, the temperature increases and decreases according to an inverse exponential curve, and the amplitude of these oscillations is related to the absorbed power and is given by the following formula:

$$\Delta T_{mod} = K.P_{abs} \quad (2)$$

Where K, depends only on film properties and modulation frequency [13], and is of the order of a few tens.

The thin film is also illuminated by two LED assemblies (to ensure homogeneous light) emitting around 535 nm, which is well-suited for exciting the fluorescence of rhodamine B, as its absorption was measured (in our ethanol solution) with a peak close to this wavelength (559 nm, Fig. 6).

Using a high-pass optical filter (>580 nm) attached to the camera lens, direct and reflected LED light is eliminated. Consequently only fluorescence light (around 600 nm, Fig. 7), and residual light from the room are recorded (usually we turn off the light; if it is not possible, the use of pulsed LED light becomes relevant, see §IV.C).

NB. It should be noted that, since the electromagnetic field has no influence on this fluorescence phenomenon, any antenna can be measured in this way.

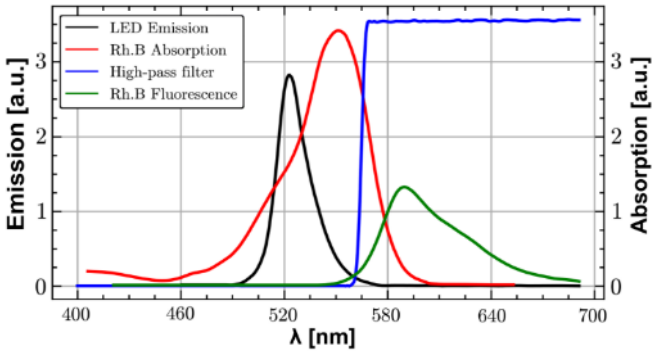

Fig. 6. Measurements of LED emission and Rhodamine B in ethanol solution spectra (absorption and fluorescence); high-pass filter.

To achieve a reliable fluorescence signal, a systematic effort has been undertaken to optimize the coating process of rhodamine [13]. Initially diluted in ethanol and subsequently blended with epoxy resin, the utilization of a film applicator has proven efficient in ensuring a consistent coating thickness of 60 µm. The process exhibits a remarkable precision, with an accuracy of ±1 µm and a limited standard deviation of 0.35 µm, which represents a ±1.67% variation maintained across a substantial surface area spanning several square decimeters. Maintaining uniformity is crucial. Any variation in coating thickness can compromise the quality of the measurement, with sensitivity decreasing in thinner areas. However, it is important to note that we measure the variation in fluorescence normalized by the fluorescence in the absence of a field. Therefore, the accuracy of the electric field measurement remains unaffected by these thickness variations.

Fluorescence variations ΔF_{mod} captured by the camera are directly proportional to the film temperature variations ΔT_{mod} , and therefore to the square of the electromagnetic field amplitude ; using (1) and (2) we obtain :

$$E = \sqrt{\frac{2}{K} Z_s \sqrt{\Delta T_{mod}}} = k\sqrt{\Delta F_{mod}} \quad (3)$$

Where k is a constant that depends only on the properties of the coated film, and lies in the range 0.05 to 0.1.

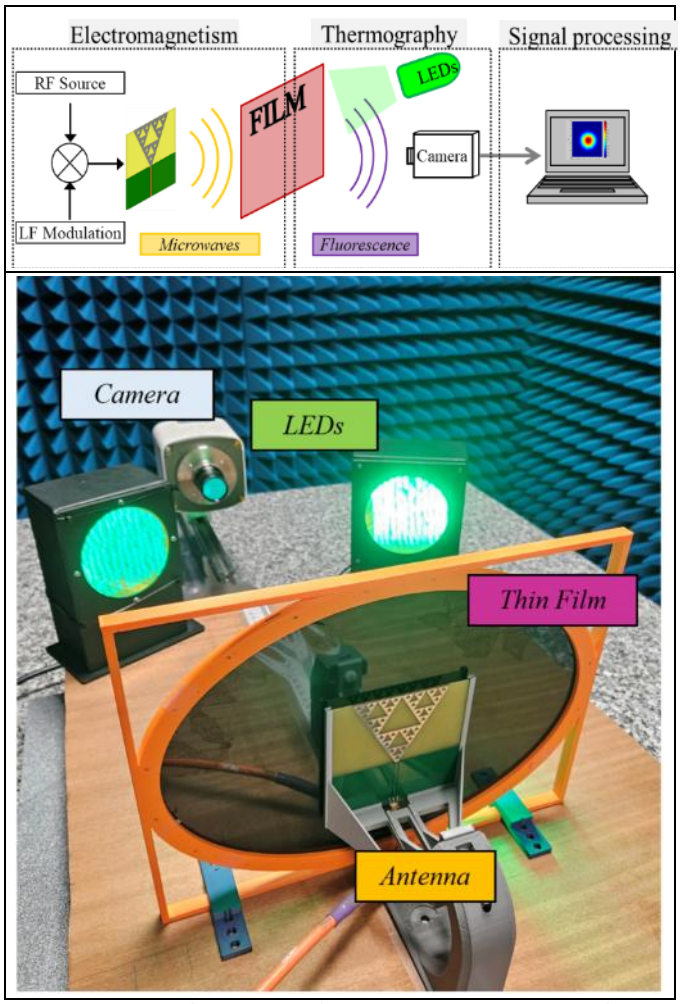

Fig. 7. Schematic of the method of measurement (top), and view of the test bench (bottom).

IV. Results: Near Field Measurements

For the presented measurements, we used a high-sensitivity monochrome sCMOS camera, the Dhyana 400D, equipped with a Gpixel GSENSE2020 sensor, which demonstrates a quantum efficiency (QE) of 72% at 595 nm. The camera, with its effective area of 13.3 mm x 13.3 mm and a resolution of 2048 by 2040 pixels, each 6.5 µm in size, captures a detailed image of the variation in the distribution of fluorescence caused by the modulated low-frequency microwaves. A frame rate of 25 frames per second (FPS) at a 16-bit depth allows for rapid acquisition of an image sequence, capturing the dynamics of the fluorescence variation with a rich data set, which is essential for rigorous temporal and spatial analysis.

The two LED assemblies are symmetrically positioned relative to the optical axis and inclined at 40 degrees, induce fluorescence without saturating the sensor, taking advantage of the camera's 86.6 dB dynamic range. The 40 ms exposure time is optimized to exploit the full dynamic range of the sensor, balancing light capture with pixel histogram, without saturation.

The camera is positioned at 54 cm from the thin film, ensuring precise spatial calibration for fluorescence measurements. The f/2.8 lens offers a sufficient aperture to capture light while providing fine spatial resolution and adequate depth of field to keep the film in focus across the entire image.

Recording almost 1000 images per sequence (this corresponds to a 40-second recording, since we have 25 FPS) constitutes a substantial database for statistical analysis of spatial and temporal variations in the fluorescence profile. Establishing a Region of Interest (ROI) on the image allows for focusing the analysis on the relevant area, increasing acquisition speed and improving the signal-to-noise ratio [15].

The size of the ABS plastic frame, designed to hold the thin film, is specifically engineered to avoid influencing fluorescence measurements. To achieve this, we made the frame (and the film) significantly larger than the active area of the antenna (Fig. 7), with dimensions of approximately 32 cm in width and 24 cm in height. This design keeps the edges of the frame away from the antenna, preventing any truncation effects.

The antenna is fed by a RF signal generator supplying a 10 W amplifier, with square low frequency (below Hz) modulation. The incident power on the antenna is measured (a broadband coupler connected to a powermeter was used). Note that measurements are normalized to a power of 1 W for comparison with HFSS simulations.

A. Continuous LED illumination

We present near-field (antenna located 10-mm far from the film) measurements at 2.68 GHz (corresponding to the second peak of the S11, see Fig. 2).

The demodulated image of the fluorescence is converted into electric field map thanks to the formula (3).

The simulated E-field map is compared with the measurements. Two (vertical and horizontal) profiles are also given, for both simulation and measurement, in order to provide a more quantitative comparison, see Fig. 8.

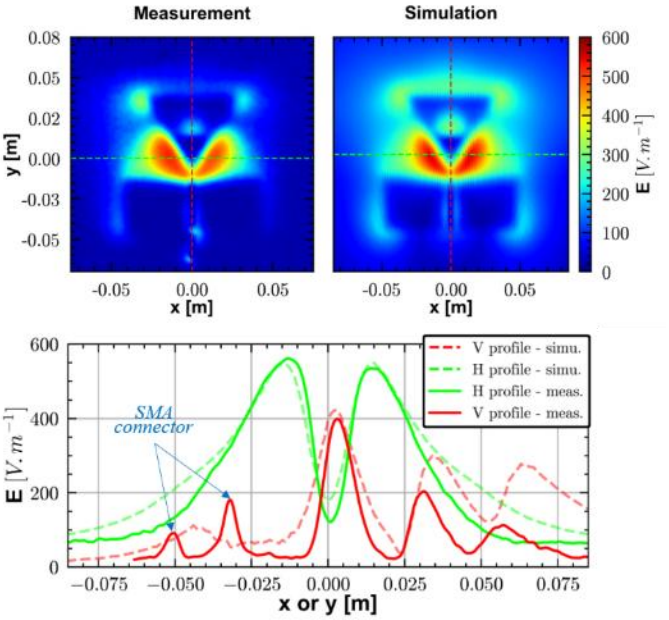

Fig. 8. Near field (@10 mm), at 2.68 GHz, comparison with simulation (continuous LEDs illumination) in ambient light.

We note a qualitative similarity between simulation and measurement. The latter shows the expected field structure, although with an underestimated level for the lowest electric field values. This illustrates the lower accuracy of the measurement for lower field level, where the signal to noise ratio decreases.

The profiles are also in good agreement, bearing in mind that the first two peaks in the measured image are due to the SMA connector, which is not represented in the simulation. These two peaks should therefore be disregarded.

It should be noted that we also carried out a measurement using the well-known EMIR (infrared thermography) method. As might be expected, the results obtained were very similar, albeit with a higher dynamic range (see Fig. 9), as the method is more mature and therefore optimized [18, 19]. This comparison was also used to calibrate our measurements.

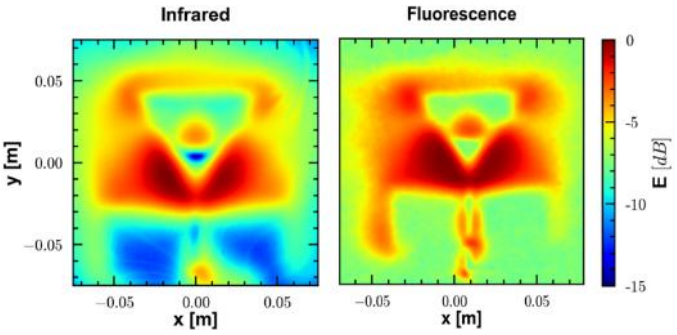

Fig. 9. Near field (@5 mm), at 2.68 GHz, comparison with infrared thermography.

As the measurement is based on fluorescent light capture, we carried out a similar measurement in a dark room, expecting an improvement in image dynamics. This was not the case (Fig. 10). This suggests that the combination of the filter (which eliminates much of the stray light) and frame-synchronous demodulation successfully isolates the useful part of the measured signal.

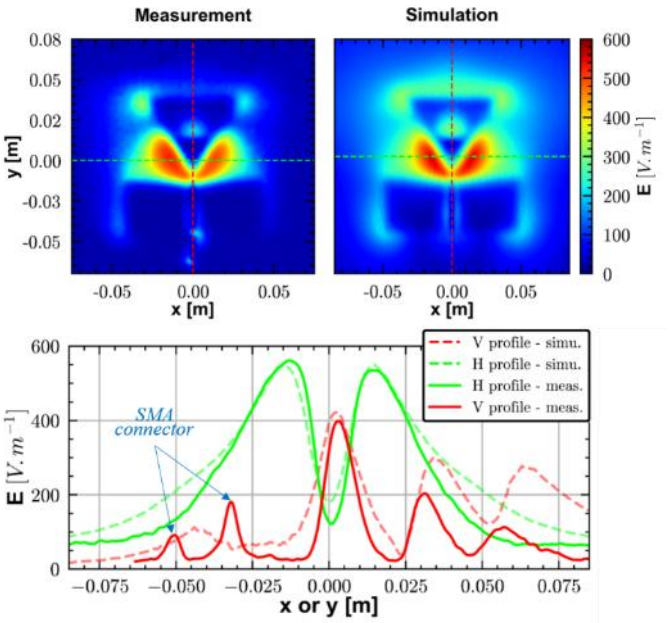

Fig. 10. Near field (@10 mm), at 2.68 GHz, comparison with simulation (continuous LEDs illumination), in dark room.

At this stage, the measurement provides mainly qualitative information. It shows how the antenna radiates, and provides a complete near-field map in just a few seconds.

B. Antenna fault detection

Fluorescence thermography may be a good way of quickly checking whether an antenna is behaving properly. Indeed, if there is a defect on the antenna, which might be difficult to identify (especially if it is located inside the substrate: a via in the case of a multi-patch antenna, for example), it will be immediately visible on the image. Note that this type of method can also be obtained using infrared thermography [20, 21]. It is interesting to note that thermo-reflectance imaging also utilizes fluorescence to reveal defects on antennas, but only through thermal frames (with high sensitivity if associated with spin-crossover materials) [22]. It, however, does not provide direct EM field visualization.

We therefore deliberately placed a defect (a strip of aluminum 20-mm long and 2-mm wide), to see its influence on the near-field structure. This appears degraded as evidenced in Fig. 11. To underline this influence, we also show the difference between images with and without defects, as well as between two images without defects but taken at different times. In the first case, we obtain a field variation of the order of 100 V/m, compared with a residual variation of less than 1 V/m in the second case (see the different scales in Figure 11, below).

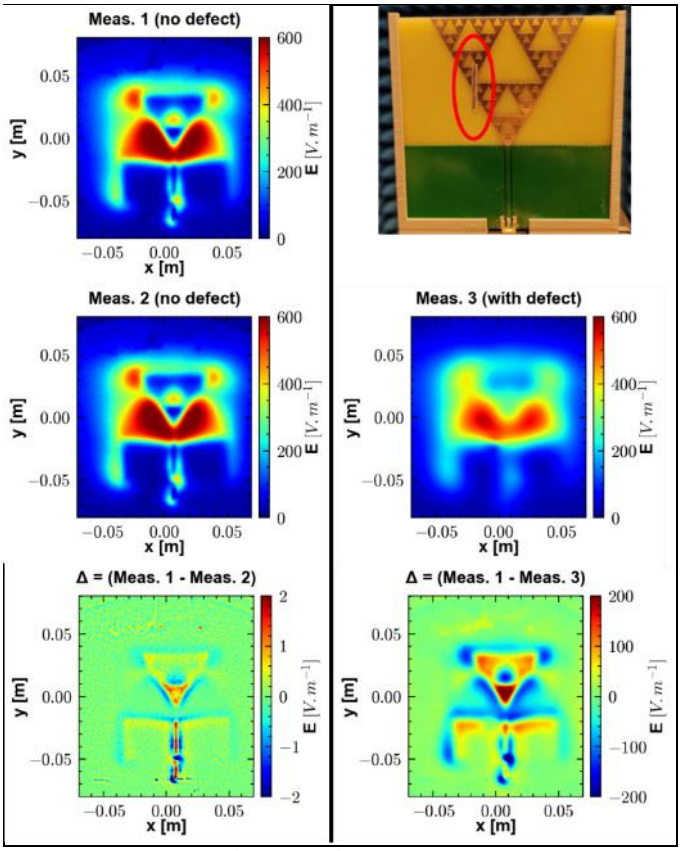

Fig. 11. Measurement of the near field (@10 mm), at 2.68 GHz, with / without a small defect on the antenna. Intermittent LED illumination (pulsed light).

C. Pulsed LED light illumination

We noticed that continuous LED illumination was responsible for a small but detectable heating of the film. Although this phenomenon is filtered out by synchronous demodulation, it slightly modifies the film behavior between the beginning ("cold film") and the end (20 to 30 seconds later) of the recording ("warm film").

For this reason, we adopted a measurement method in which the LEDs are not continuously powered but instead deliver pulsed light illumination. This is the main contribution of the present paper, as we will demonstrate that the modulation of the fluorescence signal enhances the dynamics of the E-field cartographies. The LEDs are alternately switched on and off, maintaining a 50% duty cycle, within a frequency range from 0.5 to 2 Hz.

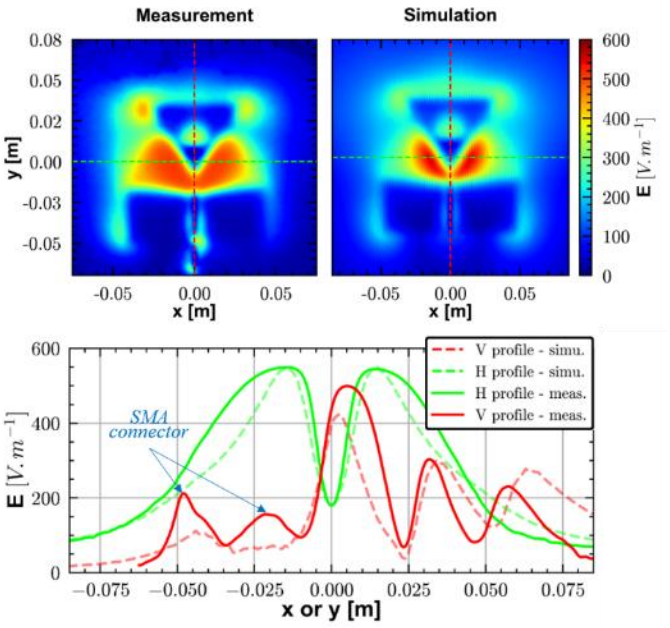

Fig. 12. Near field (@10 mm), at 2.68 GHz, with pulsed light illumination at 0.5 Hz (ambient light).

Fig. 12 (0.5 Hz pulsed illumination) shows a slight improvement over continuous illumination (Fig. 8 and 10). The profile levels in particular match the simulation better (the first two peaks still correspond to the connector, not represented in the simulation). The horizontal profile is also more accurate on the sides, but the peaks are a little wider in the measurement.

We carried out similar measurements under degraded conditions (addition of stray light) to demonstrate the improvement due to pulsed light. In fact, we imagine that this method could be used outdoors on working antennas, with uncontrolled illumination. Fig. 13a illustrates the improved near-field map (here, the antenna is closer - 5 mm -, which explains the difference in image with Fig. 8, 10, 11 and 12).

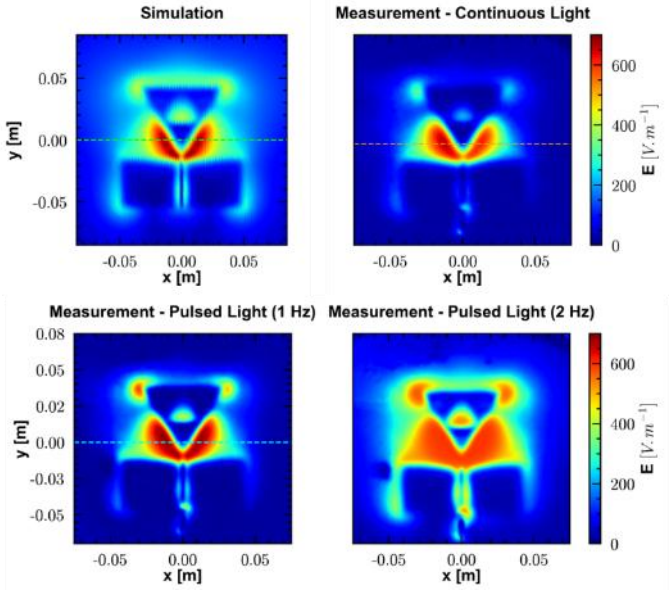

Fig. 13a. Near field (@5 mm), at 2.68 GHz; continuous and pulsed light illumination (ambient light + desk lamp).

The pulsed light profile in Fig.13b also matches the simulation better than the continuous light profile.

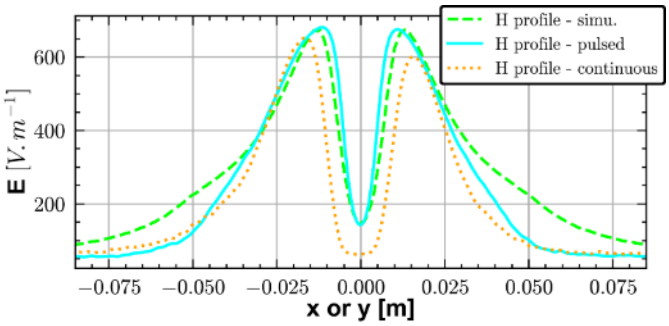

Fig. 13b. Near field (@5 mm), at 2.68 GHz; continuous and pulsed light (1 Hz) illumination (ambient light + desk lamp): horizontal profiles.

Switching from continuous to pulsed LED illumination significantly improves the measurement contrast by mitigating the heating effects observed with continuous illumination. This improvement is consistent across different conditions, including degraded scenarios, emphasizing the robustness of the pulsed illumination method. The enhanced contrast, quantified at nearly 8 dB (Fig. 14), demonstrates the efficacy of this approach in providing more accurate and reliable measurements.

We observed that the optimal conditions for pulsed illumination occur at a frequency of 1 Hz for the studied RF frequency (2.68 GHz), as shown in Fig. 13 and 14. This indicates a relationship between the two modulations (the RF source modulation, and the LED modulation), suggesting an interplay that warrants further investigation. Future work will focus on exploring this aspect to better understand the underlying mechanisms and optimize the measurement technique accordingly.

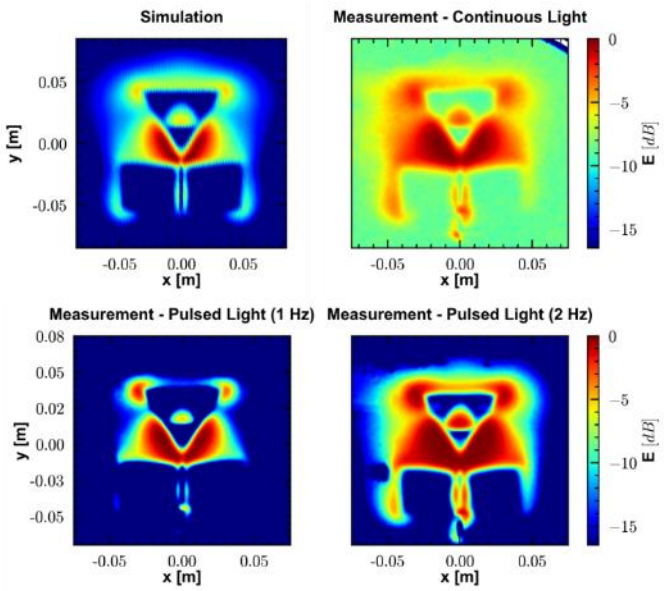

Fig. 14. Near field (@5 mm), at 2.68 GHz; continuous and pulsed light illumination (ambient light + desk lamp), in dB.

V. Conclusion

Fluorescence thermography has been used to characterize the near field of a fractal antenna, enabling the acquisition of high-resolution maps (several megapixels) within seconds.

Even though fluorescence thermography is currently limited to a dynamic range of around 15 to 20 dB, we believe this method has significant room for improvement, as demonstrated here. Additionally, the optical camera used in fluorescence thermography has low noise (especially compared to IR cameras). Moreover, fluorescence thermography allows for measurements through a porthole, which is particularly useful for certain identified applications, such as thermal testing of space antennas conducted in an oven. Lastly, this method provides high-resolution images and utilizes a common sCMOS camera. Compared to a traditional EM probe, this method allows for the rapid mapping of a surface, independent of frequency from kHz to THz, with short measurement times. It enables the visualization of the radiated field, making it a powerful tool for antenna diagnosis. Additionally, the probe can be used in the very near field, a growing area of investigation for omnidirectional antennas, which is a limitation for traditional EM probes due to strong coupling with the antenna under test. However, only the field intensity is measured by fluorescence (or infrared) thermography; the phase and vector components of the field remain unknown. This is a significant limitation for far-field reconstruction, which is required for antenna testing. This limitation could be overcome with phase retrieval algorithms.

We have demonstrated the capability to diagnose antenna behavior efficiently, allow for the rapid detection of defects. Additionally, we introduced a novel approach using pulsed light illumination of the sensor, which enhances the dynamic range of the images. This promising technique is currently under further investigation, particularly in terms of digital image filtering, and is expected to lead to significant improvements in image quality.

Furthermore, we observed that the optimal conditions for pulsed light illumination occur at a frequency of 1 Hz for the presently studied RF frequency. This finding suggests a correlation between both modulations, highlighting an area of future research. Investigating this interplay will help us better understand the underlying mechanisms and optimize the measurement technique further. This will be the focus of our upcoming work, aiming to enhance the robustness and accuracy of fluorescence thermography for antenna diagnostics.

References

[1] K. P. Slattery, J. W. Neal and Wei Cui, "Near-field measurements of VLSI devices," *IEEE Trans. on Electromagnetic Compatibility*, vol. 41, no. 4, pp. 374-384, Nov. 1999, doi: 10.1109/15.809825.

[2] E. Saenz, M. Paquay, L. Rolo; E. van der Houwen, P. Radzik, P. de Maagt, U. Klein, G. Sonnabend, D. Marote Alvarez, "Measurements of the 664 GHz feed horn for the ICI instrument of the MetOp-SG satellite," *International Symposium on Antennas and Propagation (ISAP)*, 2017.

[3] H. Halim, S. Prasad, C. Beckman, "Evaluation of a Near Field Scanner for TRP and Radiation Pattern Measurements of GSM Mobile Phones," *3rd European Conference on Antennas and Propagation (EuCAP)*, 2009.

[4] https://nexiogroup.com/en/near-field-measurement-system-bat-scan/.

[5] https://www.mvg-world.com/fr/products?category=Antenna%20Measurement.

[6] S. Arakelyan, H. Lee, A. Babajanyan, S. Kim, G. Berthiau, B. Friedman, K. Lee, "Antenna Investigation by a Thermoelastic Optical Indicator Microscope," *EEE Antennas and Propagation Magazine*, vol. 61, no. 2, pp. 27-31, April 2019, doi: 10.1109/MAP.2019.2895667.

[7] H.Lee, S. Arakelyan, B. Friedman,K. Lee, "Temperature and microwave near field imaging by thermo-elastic optical indicator microscopy," *Nature Scientific Report*, no. 6, 2016.

[8] D. Metzger, "Quantification of the thermographic mapping of microwave fields," *PhD Thesis*, Univ. of Colorado, Colorado Springs, CO, USA, 1991.

[9] J. Norgard, J. Will, C. Stubenrauch, "Quantitative images of antenna patterns using infrared thermography and microwave holography," *International Journal of Imaging Systems and Technology*, vol. 11, no. 4, pp. 210 – 218, 2000. doi:10.1002/ima.1006.

[10] P. Levesque and L. Leylekian, "Capteur de champ électromagnétique par thermographie infrarouge," *French Patent n° FR9816079*, 12/17/1998.

[11] www.anyfields.eu.

[12] S. Faure, J.F. Bobo, J. Carrey, F. Issac and D. Prost, "Sensitive Component for Device for measuring Electromagnetic Fields by Thermofluorescence, corresponding measurement and manufacturing methods," *International Patent WO 2019/063572*, 09/25/2018.

[13] S. Faure, J-F. Bobo, D. Prost, F. Issac, and J. Carrey, "Electromagnetic Field Intensity Imaging by Thermofluorescence in the Visible Range," *Phys. Rev. Applied* 11, 054084, 2019.

[14] H. Ragazzo, S. Faure, J. Carrey, F. Issac, D. Prost, J.F. Bobo, "Detection and imaging of magnetic field in the microwave regime with a combination of magnetic losses material and thermofluorescence molecules," *IEEE Trans. Magnetics*, vol. 55, no. 2, pp. 6500104, 2019, doi: 10.1109/TMAG.2018.2860520.

[15] D.L. Balageas, P. Levesque, and A. Déom, "Characterization of electromagnetic fields using lock-in IR thermography," *Thermosense XV*, SPIE vol. 1933, pp. 274-285, 1993.

[16] C. Puente-Baliarda, J. Romeu, R. Pous and A. Cardama, "On the behavior of the Sierpinski multiband fractal antenna," in *IEEE Transactions on Antennas and Propagation*, vol. 46, no. 4, pp. 517-524, April 1998, doi: 10.1109/8.664115.

[17] J.M. Gonzalez, M. Navarro, C. Puente, J. Romeu and A. Aguasca, "Active zone self-similarity of fractal-Sierpinski antenna verified using infra-red thermograms," *Electronics Letters*, vol. 35, no. 11, 1999.

[18] A. Laffont *et al*., "Near-Field Diagnosis of an X-band Telemetry Antenna using Infrared Thermography," *17th European Conference on Antennas and Propagation (EuCAP)*, Florence, Italy, 2023, pp. 1-4, doi: 10.23919/EuCAP57121.2023.10133678.

[19] A. Laffont, S. Faure and G. Mazingue, "Power Handling Test of a L-Band Antenna Using Infrared Thermography," *18th European Conference on Antennas and Propagation (EuCAP)*, Glasgow, United Kingdom, 2024, pp. 1-3, doi: 10.23919/EuCAP60739.2024.10501685.

[20] D. Prost, F. Issac, M. Romier, D. Belot, "EMIR Field Imaging for Diagnosis and Characterization of Space Antennas," *38th ESA Antenna Workshop*, ESTEC Noordwijk 2017.

[21] D. Prost, F. Issac, C. Martel, N. Capet, J. Sokoloff, O. Olivier, "Electric field imaging of a high impedance surface for GNSS array decoupling application, " *Eur. Phys. J. Appl. Phys.*, 2015.

[22] S. Wane *et al*., "Combined Thermo-Reflectance and Thin-Film Coating in Near-Field Imaging of Chip-Package-PCB-Antenna Modules for Industrial-Testing and Failure Analysis," *2023 IEEE Texas Symposium on Wireless and Microwave Circuits and Systems (WMCS)*, Waco, TX, USA, 2023, pp. 1-6, doi: 10.1109/WMCS58822.2023.10194284.